Resource limitation modulates the fate of dissimilated nitrogen in a dual-pathway Actinobacterium

David C. Vuono[1,6], Robert W. Read[1], James Hemp[2], Benjamin W. Sullivan[3], John A. Arnone III[1], Iva Neveux[1], Bob Blank[4], Carl Staub[5], Evan Loney[1], David Miceli[1], Mari Winkler[6], Romy Chakraborty[7], David A. Stahl[6], Joseph J. Grzymski[1,*]

[1]Division of Earth and Ecosystem Sciences, Desert Research Institute, Reno, NV 89512, USA

[2]Division of Geological and Planetary Sciences, California Institute of Technology, Pasadena, CA, USA

[3]Department of Natural Resources and Environmental Science, University of Nevada, Reno, NV 89557, USA

[4]Agricultural Research Service, U.S. Department of Agriculture, Reno, NV, 89512, USA

[5]Agtron, Inc. 9395 Double R Blvd, Reno, NV 89521, USA

[6]Department of Civil and Environmental Engineering, University of Washington, Seattle, WA, 98195, USA

[7]Lawrence Berkeley National Laboratory, Berkeley, CA, 94729, USA

[*]Correspondence: Joseph J. Grzymski, Division of Earth and Ecosystem Sciences, Desert Research Institute, Reno, 2215 Raggio Parkway, NV 89512, USA

Email: Joe.Grzymski@dri.edu

Abstract

Respiratory ammonification and denitrification are two evolutionarily unrelated dissimilatory nitrogen (N) processes central to the global N cycle, the activity of which is thought to be controlled by carbon (C) to nitrate (NO_3^-) ratio. Here we find that *Intrasporangium calvum* C5, a novel menaquinone-based dual-pathway denitrifier/respiratory ammonifier, disproportionately utilizes ammonification rather than denitrification when grown under carbon or nitrate limitation, not C:NO_3^- ratio. Instead, C:NO_3^- ratio is a confounding variable for resource limitation. We find that the protein atomic composition for denitrification modules (NirK) are significantly cost minimized for C and N compared to ammonification modules (NrfA), indicating that resource limitation is a major selective pressure imprinted in the architecture of these proteins. The evolutionary precedent for these findings suggests ecological and biogeochemical importance as evidenced by higher growth rates when *I. calvum* grows predominantly using its ammonification pathway and by assimilating its end-product (ammonium) for growth under ammonium-deplete conditions. Genomic analysis of *I. calvum* further reveals a versatile ecophysiology to cope with nutrient stress and redox conditions. Metabolite and transcriptional profiles during growth indicate that transcript abundances encoding for its nitrite reducing enzyme modules, NrfAH and NirK, significantly increase in response to nitrite production. Mechanistically, our results suggest that pathway selection is driven by intracellular redox potential (redox poise), which may be lowered during resource limitation, thereby decreasing catalytic activity of upstream electron transport steps needed for denitrification enzymes. Our work advances our understanding of the biogeochemical flexibility of N-cycling organisms, pathway evolution, and ecological food-webs.

Introduction

Globally, respiratory ammonification and denitrification are vital nitrogen (N) dissimilation pathways that either retain reactive N to support net primary productivity or close the N-cycle through the release of gaseous N, respectively [1]. The environmental controls on these two pathways, particularly the ratio of electron-donor to electron-acceptor (e.g., C:NO_3^-) [2], have gained attention [3–7] due to increased anthropogenic N inputs into the environment [8]. However, the effects of resource limitation on growth and pathway selection (i.e., allocation of C

48 and N to dissimilatory and assimilatory processes), which are often confounded by C:NO_3^- ratio,
49 have not been tested. Strong selective pressures from Earth's shifting biogeochemistry and
50 oxidation-state have driven evolutionary adaptions to microbial electron transport chains (ETC)
51 [9, 10], respiratory chain redox potentials [11–13], and protein atomic composition [14, 15], may
52 shed light on how these pathways are regulated in contemporary organisms. Here, by identifying
53 the biochemical and evolutionary differences between respiratory ammonification and
54 denitrification, we disentangle the ecological significance and molecular mechanisms of electron
55 transfer through either pathway in a dual pathway organism.

56 From a biochemical standpoint, the primary difference between respiratory ammonification and
57 denitrification is their respective source of reducing equivalents in the ETC: 1) heme-based
58 cytochrome c nitrite reductase used in respiratory ammonification receive electrons directly from
59 the quinone (Q) pool [16] while 2) copper and cd_1 nitrite reductases used in denitrification
60 receive electrons from a soluble electron carrier (e.g., cytochrome c) via the bc_1 complex [17].
61 From an evolutionary standpoint, we can place each N-module's origin to a putative time in
62 Earth history based on the metal co-factors that would have been bioavailable: heme-based
63 cytochromes in an ancient, more reduced, environment compared to the copper-containing nitrite
64 reductases in an oxidizing environment [18]. The bioenergetic chains of microorganisms also
65 underwent selective pressure to shift from low-potential (LP) to high-potential (HP) quinones in
66 response to Earth's oxygenation [11, 12]. Menaquinone (MK) is thought to be the ancestral type
67 of LP quinone [19]. Organisms that use ubiquinone (UQ) are thought to have evolved under high
68 O_2 tensions with α-, β-, γ-proteobacteria as the only bacterial clades to use UQ [12]. Surprisingly,
69 our understanding for the biochemistry of denitrification is based predominantly on HP UQ-
70 based systems [20], leaving a significant knowledge gap in the physiology and biochemistry of
71 LP MK-based denitrifiers and how they link electron transfer with energy capture under resource
72 limitation [21–23].

73 In order to resolve the mechanisms of C:NO_3^- control on pathway selection and better understand
74 branched respiratory chains in LP-based nitrate-reducing organisms, we undertook the
75 characterization of the novel Gram-positive Actinobacterium strain *Intrasporangium calvum* C5:
76 a dual-pathway nitrite reducer that uses MK as sole pool quinone. Here we show that over a
77 range of C:NO_3^- ratios, duplicated at two substrate concentrations, *I. calvum* disproportionately

78 utilizes its ammonia-forming pathway during C limitation (≤ 0.4mM lactate), when C:NO_3^- ratios
79 are < 1 (an observation contrary to the current paradigm). Using a genome-guided approach
80 coupled to time-series transcriptomics and metabolite profiles, we identified differentially
81 expressed genes in the bacterium's ETC and central metabolic pathways. Using this information
82 to inform a metabolic reconstruction of the ETC and extensive literature on the biochemistry of
83 the bc_1 complex, we propose a new mechanism by which these two pathways are regulated at the
84 biochemical level.

85 **Materials and Methods**

86 **Culture Conditions**

87 Media preparation: All cultures were grown at 30 ºC and shaken at 250 rpm. Nitrate reducing
88 minimal media was prepared with the following final concentrations: NaCl (0.6mM), NH_4Cl
89 (1.75mM) (for ammonium replete conditions but not used in NH4-deplete conditions), MgCl2
90 (0.2mM), CaCl2 (0.04mM), KCl (0.1mM), K2HPO4 (0.01mM), NaHCO3- (0.3mM), cysteine
91 (1mM) as reducing agent, resazurin as redox indicator, and trace elements and trace vitamin
92 solutions as reported [24, 25]. 1M sterile filtered (0.2µm) Concentrated stocks of 60% w/w
93 sodium DL-lactate solution (Sigma-Aldrich, St. Louis, MO, USA), sodium-nitrate and sodium-
94 nitrite (≥99%, Fisher Scientific, Pittsburg, PA, USA) were diluted into media prior to
95 autoclaving to achieve the desired C:NO_3^- ratio. C:NO_3^- ratio was calculated based on [3] where
96 the number of C atoms (n) in the e-donor is multiplied by the concentration of the e-donor,
97 divided by the number of N atoms in the e-acceptor multiplied by the concentration of the e-
98 acceptor (Table S4). See SI Materials and Methods for complete description of Hungate
99 technique prepared media. Mean pH for all culture vessels (time series and end-point; Table S5),
100 measured at the end of each experiment, was 7.3±0.05 (n=144).

101 **Analytical procedures**

102 Growth Curve/Cell counts/Yield Measurements: Growth curves were measured from scratch-
103 free Balch-tubes grown cultures using an automated optical density reader at OD_{600} nm
104 (Lumenautix LLC, Reno, NV). End-point cultures were monitored until all replicates reached
105 stationary phase (65-100 hours depending on C:NO_3^- treatment) (Figure S6). Cell counts were
106 performed by fixing cells in 4% paraformaldehyde (final concentration) for 20 minutes, filtered

onto 0.2μm pore-sized black polycarbonate filters. A complete description is provided in SI Materials and Methods. Biomass concentrations were measured by filtration and drying as per standard protocol [26]. A complete description is provided in SI Materials and Methods.

Ion and Gas Chromatography Measurements: A dual channel Dionex ICS-5000+ (Thermo Scientific) ion chromatograph (IC) was used to measure organic (lactate, acetate, and formate) and inorganic (nitrite and nitrate) anions on an AS11-HC column and cations (ammonium) on a CS-16 column from the bacterial growth media. A complete description is provided in SI Materials and Methods.

Phylogenetic, Genomic, and Transcriptomic Analysis

Genomic DNA was assembled using Canu (version 1.7.1) with an estimated genome size of 5 million base pairs [27]. The resulting single contiguous fragment was aligned to the *I.* calvum 7KIP genome (Acc: NC_014830.1) to compare sequence similarity in Mauve[28, 29]. Genome annotation for C5 was performed through the NCBI Prokaryotic Genome pipeline (www.ncbi.nlm.nih.gov/genome/annotation_prok/). Additional gene prediction analysis and functional annotation was performed by the DOE Joint Genome Institute (JGI) using the Isolate Genome Gene Calling method (Prodigal V2.6.3 February, 2016) under the submission ID 172966. The complete genome sequence and annotation is available in the NCBI database under the BioProject number PRJNA475609. A complete description of the phylogenetic, pathway analysis, and cost-minimization calculations is provided in SI Material and Methods. For transcriptomic analysis, the resulting raw reads were inspected using FastQC [30] to determine quality, read length, and ambiguous read percentage. Reads were trimmed based on quality score with a sliding window of 5 base pairs, quality cutoff of 28, trailing cutoff quality score of 10, as well as adapter contamination removal in Trimmomatic [31]. A complete description is provided in SI Materials and Methods. Statistical analyses were conducted in the R environment for statistical computing (r-project.org). Data that was tested using parametric statistical analysis were first validated for normality by visualizing the data as a histogram and testing via Shapiro-Wilks test for normality.

Results

136 **Genomic analysis of *I. calvum* C5.** We sequenced and analyzed the genome of *I. calvum* C5 to
137 first compare its similarity to the type species *I. calvum* 7KIP. We identified a high degree of
138 sequence similarity to 7KIP based on three homologous sequence regions as locally collinear
139 blocks (SI Results). Genome size of C5 was 4,025,044 base pairs (bp), only 662 bp longer than
140 7KIP. Genomic analysis of the ETC revealed the typical suite of complexes common to
141 facultative aerobes, including primary dehydrogenases (*nuo* complex, succinate dehydrogenase),
142 alternative *NDH-2* NADH dehydrogenase, cytochrome bc_1 complex, high-oxygen adapted
143 cytochrome c oxidase (A-family), and low-oxygen adapted cytochrome *bd* oxidase. The bc_1
144 complex subunits are also located immediately upstream of cytochrome c oxidase, suggesting
145 that these enzymes are encoded in a single operon creating a supercomplex. Despite *I. calvum*'s
146 seeming propensity for aerobic growth on a number of growth media [32], its bioenergetic
147 system uses MK as its sole pool quinone. *I. calvum* also possesses multiple pathways for
148 supplying electrons into the MK-pool, such as formate, malate, hydroxybutyrate, and
149 glycerophosphate dehydrogenases. Once in the MK-pool, there are alternative pathways for
150 MKH_2 oxidation that can circumvent the bc_1 complex, such as a membrane-bound respiratory
151 nitrate reductase module (NarG). In addition, to NarG, its dissimilatory N module composition
152 consists of a truncated denitrification pathway (N_2O is a terminal product) using a copper nitrite
153 reductase NirK and quinol-dependent nitric oxide reductase qNor. *I. calvum* also possesses both
154 catalytic and membrane anchor subunits (NrfA and NrfH, respectively) for a pentaheme
155 cytochrome c module involved in respiratory nitrite ammonification.

156 ***I. calvum* encodes for a functional NrfAH complex and assimilates NH_4^+ via respiratory**
157 **nitrite ammonification.** To gain insight into possible function of the NrfAH complex, we
158 aligned the NrfA protein sequences from C5 and 7KIP to a collection of 33 recognized
159 cytochrome c nitrite reductases from published annotated genomes (Table S1). This confirmed
160 that NrfA from *I. calvum* is a member of the CxxCH 1st heme motif group (Figure 1A), which
161 forms one of four clades on the NrfA phylogenetic tree. We then queried the genomes of the taxa
162 in our phylogeny for other annotated N-reducing modules used in nitrate reduction, nitrite
163 reduction, NO-forming nitrite reduction, and primary pool quinone. Among the three major
164 clades of NrfA, at least 5 additional taxa are noted having dissimilatory N-module inventories
165 containing dual respiratory pathways: *S. thermophilum, B. azotoformans, B. bataviensis*, *B.*
166 *bacteriovorus*, and *Candidatus* N. inopinata, (Figure 1A). None of the taxa in our NrfA

167 phylogeny harbored the cd_1 nitrite reductases (NirS). Due to the exclusive NirK representation in
168 dual-pathway membership, we asked whether there might be differences in protein atomic
169 composition between NirK and NrfA, given the disparate evolutionary origins of these modules
170 [33]. We collected 20 additional publicly available NirK protein sequences from nondual-
171 pathway denitrifiers (Table S1) and calculated the protein C and N composition for our
172 NirK/NrfA collection as atoms per residue side-chain (Figure 1B). These results showed a
173 significant depletion in C and N atoms per residue side-chain (ARSC) for NirK compared to
174 NrfA (C and N: $p<0.001$; t-test), indicating that resource constraints are imprinted on the
175 evolution of these proteins.

176 We next tested the functionality of *I. calvum*'s Nrf complex by growing the bacterium under
177 reducing conditions (8 mM lactate, 12 mM nitrate, ammonium-replete). We then performed a
178 state-transition where biomass from late-exponential growth phase was collected and
179 anaerobically inoculated into ammonia-deplete media (Figure 1C; SI Results). Despite no
180 detectable amounts of ammonium produced in the media over time, cell counts increased
181 $5.4x10^5 \pm 8.9x10^4$ cells/mL (0.126±0.02 optical absorbance at OD_{600}) over a 48-hour incubation,
182 indicating consumption of ammonium produced by NrfA. Net ammonium production was
183 13±2.7 µmoles with the remainder of dissimilated N being used by the denitrification pathway
184 (24±4.2 µmoles N_2O-N), resulting in a recovery of 97.4% dissimilated N. These results
185 confirmed that *I. calvum* C5 has a functional Nrf complex and also consumes the product
186 (ammonium) of respiratory nitrite ammonification.

187 **Respiratory nitrite ammonification exceeds denitrification under C-limitation.** We
188 investigated C:NO_3^- control on respiratory ammonification versus denitrification on cultures of *I.*
189 *calvum* C5 over a high resource C:NO_3^- range (16-0.4 mM lactate, 12 mM nitrate; ratio 4-0.1)
190 and low resource C:NO_3^- range (1.6-0.04 mM lactate, 1.2 mM nitrate; ratio 4-0.1). This
191 experimental design enabled us to evaluate C:NO_3^- control over a broader range than previous
192 studies that only considered ratios ≥ 1.5 [3, 4, 34], while also testing the effects of resource
193 concentration on pathway selection. Under all the treatments tested, gas and ion chromatography
194 measurements showed products of both respiratory pathways, differing only in the relative
195 fraction of N_2O versus ammonium production across treatments (Figure 2). At high resource
196 concentrations, respiratory ammonification did not prevail at high C:NO_3^- ratios (Figure 2A,

197 Figure 2B, left panels; Table S2). Instead, significantly greater amounts of N_2O were produced
198 over ammonium, though nitrite was still the major extracellular end-product of nitrate
199 respiration. Despite the predominance of N_2O production under the high resource concentrations,
200 ammonium production exceeded N_2O production only at the lowest C:NO_3^- ratio (0.4 mM
201 lactate, ratio=0.1) (Figure 2) and accounted for 76.2±0.1% of dissimilated N.

202 Results from the low resource dataset provided weak support for the strict stoichiometry
203 hypothesis that C:NO_3^- controls pathway selection. Ammonia exceeded N_2O production only
204 under one high C:NO_3^- ratio treatment (ratio=4; 1.6 mM lactate; Figure 2A, Figure 2B, right
205 panels). However, at ratios ≤1 (≤0.4 mM lactate), significantly more ammonium than N_2O was
206 produced. On average, respiratory ammonification accounted for 78.1±8.9% of dissimilated N
207 for lactate concentrations ≤0.4 mM. When these results are taken in context with cell physiology,
208 we observed a significant and positive relationship between specific growth rate (μ) and the
209 fraction of N dissimilated by respiratory ammonification (R^2=0.5; p<0.001) (Figure 2C, S1;
210 Table S3).

211 **Resource concentration influences the metabolite profiles of ammonium and N_2O**
212 **production.** Given the co-occurrence of end products from both pathways during the end-point
213 experiments (Figure 2), we next investigated the timing of ammonium and N_2O production
214 relative to metabolite profiles for lactate, nitrate/nitrite, and growth phase at two resource
215 concentrations with the same ratio (8 mM and 0.8 mM lactate, ratio=2; Figure 1A, Figure S2,
216 Figure S3). Despite ample e-donor and e-acceptor available for growth, the high resource
217 cultures entered a quasi-stationary phase at ~50 hours, after which there was continued slow
218 growth (Figure 1A). Metabolite profiles showed that ammonium and N_2O production began
219 simultaneously, as soon as nitrite was produced from nitrate reduction. The low resource cultures
220 entered stationary phase at ~40 hours (Figure S2) after nitrate had been fully utilized. No further
221 cell growth was observed after stationary phase was reached. These results show that cell growth
222 occurred primarily on the reduction of nitrate, while nitrite reduction to ammonium and N_2O
223 occurred during a stationary growth phase, demonstrating that microbial activity is not always
224 correlated with growth. The metabolite profiles for ammonium and N_2O at low resources (Figure
225 S2) did not mirror those observed at high resources (Figure 2A). The rate of N_2O production
226 significantly decreased and ammonium production oscillated rather than steadily increase

227 through time. These differences in metabolite profiles, further demonstrate that concentration
228 influences the activities of pathway bifurcation. Repeated time series experiments that were
229 extended up to 300 hours show that nitrite is slowly depleted, but does not get fully consumed
230 (Figure S3). When cultures were given nitrite, instead of nitrate as a terminal electron acceptor (8
231 mM lactate, 12 mM nitrite; ratio=2), we observed no immediate growth (as was observed with
232 nitrate) but measured more N_2O than ammonium production (33.4±4.8 µmoles N_2O-N and
233 8.0±2.5 µmoles NH_4^+, respectively) (Figure S4), demonstrating respiratory ammonification does
234 not exceed denitrification when nitrite is supplied as the sole acceptor in *I. calvum*.

235 **Nitrite-reducing modules are up-regulated during late exponential- and stationary-phase**
236 **growth.** In order to gain insight into mechanisms of gene regulation and transcriptional
237 organization of *I. calvum*, we conducted RNA-Seq in parallel with the high resource time-series
238 metabolite profile (Figure 3A). This approach enabled us to compare genome-wide differential
239 expression based on $\log_2$ fold change (lfc) of RNA extracted from three growth phases: early
240 exponential (EE), late exponential (LE), and stationary (ST) (Figure 3B, Figure S5). Within the
241 central metabolic pathway beginning with the conversion of lactate to pyruvate, we observed a
242 moderate decrease in transcript abundance of L-lactate dehydrogenase (LDH) (Intca_16740)
243 between EE-LE and -ST (lfc = -1.6±0.7; -1.9±0.7), respectively. Lactate utilization protein C
244 (LUP) (Intca_04080), an enzyme involved in lactate degradation, also showed a moderate and
245 significant decrease in transcript abundance between EE-LE and -ST (lfc = -1.6±0.6; -2.4±0.6,
246 p=0.002), respectively. *I. calvum* encodes for two parallel metabolic pathways for pyruvate
247 conversion to acetyl-CoA: pyruvate dehydrogenase (PDH) (Intca_01255) and pyruvate
248 ferredoxin oxidoreductase (PFOR) (Intca_15510). For PDH, there was a significant and
249 moderate increase in transcript abundance between EE-LE and -ST (lfc = 2.1±0.6, p=0.002;
250 1.5±0.6), respectively. For PFOR, there was a minor decrease in transcript abundance between
251 EE-LE (lfc = -0.43±0.5), and then a moderate increase in transcript abundance between EE-ST
252 (1.1±0.5). Citrate synthase (Intca_04135), the enzyme catalyzing the conversion of acetyl-CoA
253 to citrate and the first step of the tricarboxylic acid (TCA) cycle, showed a highly significant
254 increase in transcript abundance between EE-LE and -ST (lfc = 4.3±0.5, p<0.001; 6.9±0.5,
255 p<0.001).

256 Within the ETC, there was moderate and significant decrease in transcript abundance for all
257 subunits from the primary dehydrogenase (*nuo* complex; Intca_03465-03539) between EE-LE
258 and -ST (lfc = -1.2±0.3; -2.4±0.6, $p<0.001$), respectively. Nitrate reductase subunits showed no
259 change in transcript abundance between EE-LE (lfc = 0.01±0.07) and moderately decreased in
260 abundance by ST (lfc = -1.2±0.1), which was corroborated by the depletion of nitrate during
261 stationary phase. There was a significant increase in transcript abundance of *nirK* (Intca_17170)
262 (lfc = 2.2±0.6, $p=0.003$; 2.4±0.6, $p<0.001$) and quinol dehydrogenase/membrane anchor subunit
263 *nrfH* (Intca_09465) (lfc = 2.5±0.6, $p=0.001$; 2.1±0.6, $p=0.003$) by EE-LT and EE-ST,
264 respectively, which coincided with nitrite production (Figure 3A). The catalytic subunit of the
265 cytochrome c nitrite reductase complex (*nrfA*) (Intca_09460) also increased moderately in
266 transcript abundance by EE-LT and EE-ST (lfc = 1.6±0.6; 1.0±0.6), respectively (Figure 3B).
267 Contrary to the transcript abundance patterns of *nirK* and *nrfAH*, nitric oxide reductase (qNor;
268 Intca_01525) transcripts moderately increased between EE-LT (lfc = 1.6±0.6) but decreased in
269 the successive time periods (lfc = 0.43±0.6 between EE-ST; lfc = -1.2±0.6 between LE-ST)
270 (Figure 3B).

271 There was a significant increase in transcript abundance of formate transporter *focA*
272 (Intca_17150) between EE-ST, as well as LE-ST (lfc = 4.9±0.7, $p=0.002$; 4.8±0.7, $p=0.002$;
273 respectively). We verified the production of formate in our ion chromatography measurements in
274 the range of 100-200μM following late exponential growth. We also observed a moderate
275 increase in transcript abundance of formate dehydrogenase (FDH) subunits (Intca_11150-
276 11160). These results implicate the activity of formate oxidation, which would contribute to a Δp
277 in the periplasm via a Q-loop mechanism and the reduction of MK for electron transfer to nitrite
278 via cytochrome c nitrite reductase. Considering that formate was not provided in our media
279 recipe, an alternative pathway for formate production must exist in *I. calvum*. We also observed
280 acetate production in similar concentrations as formate (100-200μM). In *E. coli*, formate is
281 produced anaerobically from the action of pyruvate formate lyase (PFL). We identified a putative
282 PFL based on genome annotation (Intca_12230), where transcript abundance also significantly
283 increased by ST. PFL is also highly sensitive to oxygen [35], which was also in agreement with a
284 significant increase in transcript abundance between EE-ST and LE-ST (Figure 3B) of
285 cytochrome *bd* oxidase (Intca_01110 and Intca_01115), which is thought to protect anaerobic
286 enzymes against oxidative stress [36].

287 **Discussion**

288 We challenge the paradigm that C:NO_3^- ratio controls pathway selection in a dual-pathway
289 organism based on a simple principle: ratios do not account for the abundance of growth-limiting
290 resources. We hypothesized that limitation in C or NO_3^- should better predict pathway selection
291 in a dual-pathway denitrifier/respiratory ammonifier. To test this hypothesis, we systematically
292 measured the response of the Gram-positive Actinobacterium *Intrasporangium calvum* C5 to the
293 same range of C:NO_3^- ratios at both high and low resource loadings to better resolve mechanisms
294 of pathway selection. We demonstrated that resource concentration, not C:NO_3^- ratio, influences
295 pathway selection. We found stronger support for respiratory ammonification preference under
296 C-limitation (at low C:NO_3^- ratios), which also grew at significantly higher growth rates (Figure
297 2). These results suggest that the NrfA complex, which receives electrons directly from the MK-
298 pool, is optimized to maximize power when one or more resources are limiting. The enrichment
299 of C and N ARSC in publically available NrfA over NirK protein seuqences (Figure 1B)
300 provides further support and evolutionary precedence to ammonification preference over
301 denitrification under resource limitation. This is because the end-product of ammonification can
302 be used as an assimilatory N-source (Figure 1C), indicating no evolutionary constraint to cost
303 minimize N. These data, together with metabolic reconstructions from metabolite and
304 transcriptional profiles (Figure 3), suggest that C:NO_3^- ratio alone is insufficient to explain
305 pathway selection.

306 The theoretical basis for pathway selection is explained by the law of the minimum (LM) and the
307 maximum power principle (MPP), which state that growth is limited by the least abundant
308 resource and that biological systems are designed to maximize power in order to effectively
309 allocate energy to reproduction and survival [37, 38], respectively. Here, it appears these two
310 theories are working together: when resources are limited, the cell utilizes the respiratory
311 pathway for growth that is optimized to maximize power. Power, in this case, is realized as
312 higher growth rates from the cultures exhibiting disproportionately higher ammonium production
313 than N_2O production (Figure 2: high resources: C:NO_3^- ratio = 0.1; low resources: C:NO_3^- ratios
314 = 4, 1, 0.5, 0.1). More specifically, the bacterium must generate a greater Δp in order to
315 maximize power when starved for a growth limiting resource. This may help to further explain
316 how respiratory ammonification, which is overall energetically less favorable than denitrification

317 (lactate with nitrite: ΔG^o = -763.98 versus ΔG^o = -1196.93, respectively), can have higher growth
318 yields [39] and growth rates (Figure 2, Figure S1) under C- and N-limitation due to the higher
319 energy yield on a per-nitrite basis (denitrification: -217 KJ per mole nitrite; respiratory
320 ammonification: -399 KJ per mole nitrite). For comparison, a total of 8 H^+ are translocated
321 during denitrification by *I. calvum* (not including nitrate reduction since both pathways share this
322 step) (Figure 3): NADH dehydrogenase translocates 4 H^+ per MKH_2 oxidized and the bc_1
323 complex translocates an additional 4 H^+ per MKH_2 oxidized. However, 2 H^+ must be consumed
324 in the periplasm to reduce nitrite to NO [40]. qNor has a net zero H^+ release (consumes 2 H^+ to
325 make N_2O but releases 2 H^+) without MKH_2 regeneration [41]. Thus, a net total of 6 H^+ are
326 translocated per nitrite reduced in denitrification with added biosynthetic costs of making the bc_1
327 complex and qNor. In respiratory ammonification, MK/MKH_2 redox pair is cycled between
328 NADH dehydrogenase and formate dehydrogenase. 6 electrons and 8 H^+ are needed to reduce
329 nitrite to ammonium, thus 3 MKH_2 are needed [16]. If MKH_2 is received from NADH
330 dehydrogenase, 12 H^+ are translocated plus 2 H^+ from FDH. As each MKH_2 is oxidized at the
331 binding site of NrfH, 2 H^+ are liberated [16], resulting in a net total of 12 H^+ translocated per
332 nitrite reduced for respiratory ammonification. This implies that the cell might deplete its NADH
333 pool more rapidly on a per nitrite basis. However, if more protons are pumped in the early stages
334 of growth, the cell would be allocating the ATP generated for anabolism, as evidenced by higher
335 growth rates in the cultures exhibiting higher amounts of respiratory ammonification (Figure 2),
336 which is supported by the MPP.

337 Under our high resource conditions (Figure 2; left panels), at $C:NO_3^-$ ratios ≥ 1, we observed that
338 denitrification prevailed and these cultures had lower growth rates than the predominantly
339 ammonium producing cultures. These high resource circumstances resulted in the production of
340 toxic intermediates (i.e., NO_2^- and possibly NO, albeit at undetectable levels), which may explain
341 why these cultures had lower growth rates (Figure 2; left panels) and quasi-steady state growth
342 curves in our high resource metabolite profile (Figure 3A). Rowley and colleagues [42] reported
343 that at least 20% of the N_2O released during high C conditions were produced by competition
344 between nitrite and nitrate in the active-site of NarG. Under excess C concentrations, NarG
345 produces intracellular NO from NO_2^- and these intermediates are likely inhibitory to cell growth,
346 which may explain why our growth curves (Figure 3A) reached a quasi-steady state before
347 nitrate had been fully utilized (as compared to the low resource metabolite profile, Figure S2).

348 Furthermore, resources were not limiting growth under these conditions. Rather, the cells were
349 likely experiencing toxicity from NO and NO_2^- and thus the metabolic outcomes would be
350 beyond the scope of the LM and MPP. Nonetheless, these results clearly demonstrate that end-
351 product formation from the two resource concentrations tested, with the same C:NO_3^- ratios, are
352 not identical thereby refuting the C:NO_3^- control hypothesis.

353 We selected a single treatment (8 mM lactate, 12 mM nitrate; C:NO_3^- ratio = 2), in which we
354 observed both denitrification and respiratory ammonification occurring simultaneously, for
355 RNA-Seq in order to gain insight into the transcriptional organization of actively growing *I.*
356 *calvum* cells (Figure 3). Strangely, we saw a decrease in transcript abundance encoding for two
357 enzymes known to convert lactate to pyruvate, LDH and LUP. While normalized read counts
358 (Figure S5) were generally consistent across growth phases, indicative of constitutive expression,
359 further research investigating the mode of anaerobic lactate oxidation in *I. calvum* would
360 illuminate how reducing equivalents are fed into its central metabolic pathway. For example, *S.*
361 *loihica* PV-4 is known to use lactate for both denitrification and respiratory ammonification, but
362 only uses acetate for denitrification [24]. Nonetheless, our transcriptomic data suggests that
363 pyruvate plays a central role in providing reducing equivalents to the TCA cycle as Acetyl-CoA,
364 as evidenced by significant upregulation in the genes encoding for pyruvate dehydrogenase and
365 citrate synthase, as well as apparent "leaking" via incomplete lactate oxidation through the
366 release of acetate and formate. Such leaking may be produced by a putative PFL, adding to the
367 diversity of C utilization pathways feeding the ETC, and thereby driving pathway selection for
368 nitrite reduction. Our transcriptomic results, coupled with a parallel metabolite profile (Figure 3),
369 also suggest that the dual-pathway is induced by the presence of nitrite, and is not constitutively
370 expressed like nitrate reductase, *narG*. Furthermore, it appears that the significant increase in
371 transcript abundance for the gene encoding the *bd* oxidase helps to protect the anaerobic-
372 dependent biochemical machinery against oxidative stress, thereby scavenging any residual
373 oxygen during anaerobic growth.

374 Our metabolite profiles for N oxyanion respiration and N_2O versus ammonium production show
375 conflicting patterns relative to previous studies (Figure 3A, Figure S2). Yoon and colleagues [43]
376 reported complete reduction of nitrate, production of nitrite, and then rapid consumption of
377 nitrite, with N_2O as the main end-product, by *S. loihica* PV-4 (5 mM lactate, 1 mM nitrate;

378 ratio=0.6). When Yoon and colleagues [43] replaced nitrate with nitrite as the dominant electron
379 acceptor (5 mM lactate, 1 mM nitrite, ratio=0.6), ammonification prevailed. Other research has
380 shown the same response to nitrite replacement and ammonification dominance using non-
381 fermentable C-sources (i.e., acetate) in chemostat enrichments of *Geobacter lovleyi*[44]. In our
382 work, nitrite was never fully depleted (Figure 3A, Figure S2, Figure S3) and when nitrite was
383 given as the only electron acceptor, the bacterium predominantly used denitrification but without
384 concurrent growth (Figure S4). Similar to our work, Kraft and colleagues[34] also reported
385 denitrification dominance when nitrite was supplied as the terminal acceptor. These differences
386 highlight an incomplete understanding for the molecular mechanisms underlying the framework
387 put forth by the LM and MPP.

388 A detailed look into the biochemistry of ETC complexes helps to shed light on the molecular
389 mechanisms modulating pathway bifurcation. For example, Yoon and colleagues [3]
390 demonstrated that elevated pH selects for ammonification in *S. loihica* PV-4. This phenotypic
391 response is due to a decrease in the midpoint potential of the Rieske protein at higher pH [45–
392 48]. Thus, any hindrance of electron flow through the bc_1 complex would ultimately reduce the
393 activity of downstream processes and promote alternative respiratory pathways. Nitrogen and C
394 limitation have also been shown to influence flux distributions in redox sensitive proteins,
395 including those found in electron transport [49]. A drop in the intracellular redox potential (redox
396 poise) of the cell due to resource limitation may decrease the midpoint potential of the Rieske
397 protein and reduce the activity of any downstream electron exit modules, such as NirK [50–52].
398 Thus, based on fundamental principles of protein redox chemistry and thermodynamics, it
399 becomes clear that denitrification versus ammonification are likely not modulated by an arbitrary
400 ratio of $C:NO_3^-$, but rather by thermodynamic constraints of the Q-cycle [11, 12]. The phenotypic
401 response of higher rates of denitrification over ammonification at high $C:NO_3^-$ ratios in other
402 published studies [3, 4] may also be due to enrichment bias for organisms that utilize quinones
403 with higher midpoint potentials in their bioenergetic chains (Figure 1). Bergdoll and colleagues
404 [11] suggested that comparisons of Rieske/cyt*b* complexes from organisms with high- and low-
405 potential quinones may help to reconcile the thermodynamic properties of Q-cycle function.
406 However, most of our understanding of denitrification bioenergetics is based on evolutionarily
407 recent UQ-based HP bioenergetic chains from Gram-negative *α*-, *β*-, *γ*-proteobacteria. Because *I.*

408 *calvum* uses a MK-based LP bioenergetic chain it may be possible that the differences in
409 pathway selection across treatments are unique to LP chains.

410 Piecing together the evolutionary history of the N-cycle using isotopic signatures for
411 geochemically available N module cofactors (i.e., Ni, Fe, and Mo) coupled to molecular
412 evolutionary analysis has revealed respiratory ammonification was likely a major component of
413 the Archean N-cycle [33]. Abiotic nitrite formation and depletion of ammonia through
414 photodissociation [53] would have created selective pressures for a dissimilatory N pathway that
415 also produced assimilatory N. We demonstrate that NrfA proteins are significantly enriched in N
416 compared to NirK (i.e., no evolutionary constraints to cost minimize N in the *nrfA* gene product
417 [15]) (Figure 1B) and that ammonium production (without accumulation in the medium)
418 supports growth in *I. calvum* (Figure 1C). The Nrf module is also relatively simplistic in that it
419 receives electrons directly from the quinol pool and not the bc_1 complex used in denitrification.
420 The early exit of electrons from the ETC (i.e., before reaching the bc_1 complex) suggests that Nrf
421 may have originated prior to the bc_1 complex. Furthermore, the quinol oxidation site (Q_o) of
422 cytochrome *b* contains a PDWY motif, indicative of an ancestral LP respiratory chain found in
423 many Gram-positive organisms [54]. However, there is still debate regarding the presence of a
424 cytochrome *bc* complex in the last universal common ancestor [54, 55]. Lastly, the Nrf module is
425 wired to operate via a q-loop with formate dehydrogenase whose Mo-cofactors would have also
426 been bioavailable during the Archean, further supporting an early evolution.

427 In summary, we employ a new predictive framework that accounts for the biochemistry and
428 evolutionary history of N modules, ETC complexes, and pool quinones to suggest the
429 mechanisms by which these two pathways are regulated at the molecular level. With this
430 understanding, it may be possible to extend our framework to environmental microbial
431 populations and accelerate model development across different ecosystem scales (i.e., cross-scale
432 systems biology).

433 **ACKNOWLEDGMENTS.** We thank F. von Netzer, K. Hunt, S Morales, N. Stopnisek, K. Meinhardt, W. Qin, N
434 Elliot, T. Hazen, H. Carlson, B. Ramsey, A. Murray, Z. Harrold, T. Morgan, and P. Longley for thoughtful feedback
435 and discussions. This research was supported by a grant from the Nevada Governor's Office of Economic
436 Development (JG), by the Desert Research Institute (DRI) postdoctoral research fellowship program, and in part by
437 Ecosystems and Networks Integrated with Genes and Molecular Assemblies (ENIGMA) (http://enigma.lbl.gov)—a
438 Scientific Focus Area Program at Lawrence Berkeley National Laboratory under contract number DE-AC02-

05CH11231 and funded in part by Oak Ridge National Laboratory under contract DE-AC05-00OR22725, and is based upon work supported by the U.S. Department of Energy, Office of Science, Office of Biological & Environmental Research.

Competing Interests

The authors declare no conflicts of interest

References

1. Knowles R. Denitrification. *Microbiol Rev* 1982; **46**: 43–70.

2. Tiedje JM, Sexstone AJ, Myrold DD, Robinson JA. Denitrification: ecological niches , competition and survival. *Antonie Van Leeuwenhoek* 1982; **48**: 569–583.

3. Yoon S, Cruz-García C, Sanford R, Ritalahti KM, Löffler FE. Denitrification versus respiratory ammonification: Environmental controls of two competing dissimilatory NO 3-/NO 2-reduction pathways in Shewanella loihica strain PV-4. *ISME J* 2015; **9**: 1093–1104.

4. van den Berg EM, van Dongen U, Abbas B, van Loosdrecht MC. Enrichment of DNRA bacteria in a continuous culture. *ISME J* 2015; **9**: 2153–2161.

5. Schmidt CS, Richardson DJ, Baggs EM. Constraining the conditions conducive to dissimilatory nitrate reduction to ammonium in temperate arable soils. *Soil Biol Biochem* 2011; **43**: 1607–1611.

6. Hardison AK, Algar CK, Giblin AE, Rich JJ. Influence of organic carbon and nitrate loading on partitioning between dissimilatory nitrate reduction to ammonium (DNRA) and N2 production. *Geochim Cosmochim Acta* 2015; **164**: 146–160.

7. Fazzolari É, Nicolardot B, Germon JC. Simultaneous effects of increasing levels of glucose and oxygen partial pressures on denitrification and dissimilatory nitrate reduction to ammonium in repacked soil cores. *Eur J Soil Biol* 1998; **34**: 47–52.

8. Galloway JN, Aber JD, Erisman JW, Seitzinger SP, Howarth RW, Cowling EB, et al. The Nitrogen Cascade. *Bioscience* 2003; **53**: 341.

9. Moparthi VK, Hägerhäll C. The evolution of respiratory chain complex i from a smaller last common ancestor consisting of 11 protein subunits. *J Mol Evol* 2011; **72**: 484–497.

10. Dibrova D V., Cherepanov DA, Galperin MY, Skulachev VP, Mulkidjanian AY. Evolution of cytochrome bc complexes: From membrane-anchored dehydrogenases of ancient bacteria to triggers of apoptosis in vertebrates. *Biochim Biophys Acta - Bioenerg* 2013; **1827**: 1407–1427.

11. Bergdoll L, Ten Brink F, Nitschke W, Picot D, Baymann F. From low- to high-potential bioenergetic chains: Thermodynamic constraints of Q-cycle function. *Biochim Biophys Acta* 2016; **1857**: 1569–1579.

12. Schoepp-Cothenet B, Lieutaud C, Baymann F, Verméglio A, Friedrich T, Kramer DM, et al. Menaquinone as pool quinone in a purple bacterium. *Proc Natl Acad Sci* 2009; **106**: 8549–54.

13. Soo RM, Hemp J, Parks DH, Fischer WW, Hugenholtz P. On the origins of oxygenic photosynthesis and aerobic respiration in Cyanobacteria. *Science (80-)* 2017; **355**: 1436–1440.

14. Baudouin-Cornu P, Schuerer K, Marlière P, Thomas D. Intimate evolution of proteins: Proteome atomic content correlates with genome base composition. *J Biol Chem* 2004; **279**: 5421–5428.

476 15. Grzymski JJ, Dussaq AM. The significance of nitrogen cost minimization in proteomes of marine
477 microorganisms. *ISME J* 2012; **6**: 71–80.

478 16. Einsle O, Messerschmidt A, Huber R, Kroneck PMH, Neese F. Mechanism of the six-electron reduction of
479 nitrite to ammonia by cytochrome c nitrite reductase. *J Am Chem Soc* 2002; **124**: 11737–11745.

480 17. Kraft B, Strous M, Tegetmeyer HE. Microbial nitrate respiration - Genes, enzymes and environmental
481 distribution. *J Biotechnol* 2011; **155**: 104–117.

482 18. Godfrey L V., Falkowski PG. The cycling and redox state of nitrogen in the Archaean ocean. *Nat Geosci*
483 2009; **2**: 725–729.

484 19. Nitschke W, Dracheva S. Reaction center associated cytochromes in Anoxygenic Photosynthetic Bactera.
485 In: Blankenship R, Madigan M, Bauer C (eds).1995. Kluwer Academic, Dordrecht, The Netherlands, pp
486 775–805.

487 20. Lalucat J, Bennasar A, Bosch R, Garcia-Valdes E, Palleroni NJ. Biology of Pseudomonas stutzeri.
488 *Microbiol Mol Biol Rev* 2006; **70**: 510–547.

489 21. Suharti, de Vries S. Membrane-bound denitrification in the Gram-positive bacterium Bacillus azotoformans.
490 *Biochem Soc Trans* 2005; **33**: 130–133.

491 22. Heylen K, Keltjens J, Stein LY. Redundancy and modularity in membrane-associated dissimilatory nitrate
492 reduction in Bacillus. *Front Microbiol* 2012; **3**: 1–27.

493 23. Decleyre H, Heylen K, Bjorn T, Willems A. Highly diverse nirK genes comprise two major clades that
494 harbour ammonium-producing denitrifiers. *BMC Genomics* 2016; **17**: 1–13.

495 24. Yoon S, Sanford RA, Löffler FE. Shewanella spp. Use acetate as an electron donor for denitrification but
496 not ferric iron or fumarate reduction. *Appl Environ Microbiol* 2013; **79**: 2818–2822.

497 25. Hillesland KL, Lim S, Flowers JJ, Turkarslan S, Pinel N, Zane GM, et al. Erosion of functional
498 independence early in the evolution of a microbial mutualism. *Proc Natl Acad Sci* 2014; **111**: 14822–14827.

499 26. APHA. Standard Methods for the Examination of Water and Wastewater, 23rd ed. 2012. American Public
500 Health Association: Washington, DC.

501 27. Koren S, Walenz BP, Berlin K, Miller JR, Bergman NH, Phillippy AM. Canu : scalable and accurate long- -
502 - read assembly via adaptive k - - - mer weighting and repeat separation. *Genome Res* 2017; 1–35.

503 28. Darling ACE, Mau B, Blattner FR, Perna NT. Mauve : Multiple Alignment of Conserved Genomic
504 Sequence With Rearrangements. *Genome Res* 2004; **14**: 1394–1403.

505 29. Darling AE, Mau B, Perna NT. Progressivemauve: Multiple genome alignment with gene gain, loss and
506 rearrangement. *PLoS One* 2010; **5**: e11147.

507 30. Andrews S. FastQC: A quality control tool for high throughput sequence data. *Available online at: http://*
508 *www.bioinformatics.babraham.ac.uk/projects/fastqc* 2010.

509 31. Bolger AM, Lohse M, Usadel B. Trimmomatic: A flexible trimmer for Illumina sequence data.
510 *Bioinformatics* 2014; **30**: 2114–2120.

511 32. Kalakoutskii LV, Kirillova IP, Krassilnikov NA. a New Genus of the. *J Gen Microbiol* 1967; **48**: 373-79–
512 85.

513 33. Klotz MG, Stein LY. Nitrifier genomics and evolution of the nitrogen cycle. *FEMS Microbiol Lett* 2008;
514 **278**: 146–156.

515 34. Kraft B, Tegetmeyer HE, Sharma R, Klotz MG, Ferdelman TG, Hettich RL, et al. The environmental
516 controls that govern the end product of bacterial nitrate respiration. *Science (80-)* 2014; **345**: 676–679.

517 35. Abbe KS, Takahashi S, Yamada T. Invovlement of oxygen-sensitive pyruvate-formate lysase in mixed-acid
518 fermetnation by Streptococcus mutans under strictly anerobic conditions. *J Bacteriol* 1982; **152**: 175.

519 36. Das A, Silaghi-Dumitrescu R, Ljungdahl LG, Kurtz DM. Cytochrome *bd* oxidase, oxidative stress, and
520 dioxygen tolerance of the strictly anaerobic bacterium *Moorella thermoacetica*. *J Bacteriol* 2005; **187**:
521 2020–2029.

522 37. Lotka AJ. Contribution to the Energetics of Evolution. *Proc Natl Acad Sci* 1922; **8**: 147–151.

523 38. DeLong JP. The maximum power principle predicts the outcomes of two-species competition experiments.
524 *Oikos* 2008; **117**: 1329–1336.

525 39. Strohm TO, Griffin B, Zumft WG, Schink B. Growth yields in bacterial denitrification and nitrate
526 ammonification. *Appl Environ Microbiol* 2007; **73**: 1420–1424.

527 40. Zumft WG. Cell biology and molecular basis of denitrification. *Microbiol Mol Biol Rev* 1997; **61**: 533–616.

528 41. Hemp J, Gennis RB. Diversity of the Heme-Copper Superfamily in Archaea: Insights from Genomics and
529 Structural Modeling. In: Schäfer G, Penefsky HS (eds). *Results and Problems in Cell Differentiation*. 2008.
530 Springer Science+Business Media, pp 1–28.

531 42. Rowley G, Hensen D, Felgate H, Arkenberg A, Appia-ayme C, Prior K, et al. Resolving the contributions of
532 the membrane-bound and periplasmic nitrate reductase systems to nitric oxide and nitrous oxide production
533 in Salmonella enterica serovar Typhimurium. *Biochem J* 2012; **762**: 755–762.

534 43. Yoon S, Sanford RA, Löffler FE. Nitrite control over dissimilatory nitrate/nitrite reduction pathways in
535 Shewanella loihica strain PV-4. *Appl Environ Microbiol* 2015; **81**: 3510–3517.

536 44. van den Berg EM, Rombouts JL, Kuenen JG, Kleerebezem R, van Loosdrecht MCM. Role of nitrite in the
537 competition between denitrification and DNRA in a chemostat enrichment culture. *AMB Express* 2017; **7**:
538 1–7.

539 45. Link TA, Hagen WR, Pierik AJ, Assmann C, von Jagow G. Determination of the redox properties of the
540 Rieske cluster of bovine heart bc1 complex by direct electrochemistry of a water- soluble fragment.
541 *EurJBiochem* 1992; **208**: 685–691.

542 46. Ugulava NB, Crofts AR. CD-monitored redox titration of the Rieske Fe-S protein of Rhodobacter
543 sphaeroides: pH dependence of the midpoint potential in isolated bc1 complex and in membranes. *FEBS Lett*
544 1998; **440**: 409–413.

545 47. Zu Y, Couture MMJ, Kolling DRJ, Crofts AR, Eltis LD, Fee JA, et al. Reduction Potentials of Rieske
546 Clusters: Importance of the Coupling between Oxidation State and Histidine Protonation State. *Biochemistry*
547 2003; **42**: 12400–12408.

548 48. Trumpower BL. Cytochrome bc1 complexes of microorganisms. *Microbiol Rev* 1990; **54**: 101–129.

549 49. Ansong C, Sadler NC, Hill EA, Lewis MP, Zink EM, Smith RD, et al. Protein redox dynamics during light-
550 to-dark transitions in cyanobacteria and impacts due to nutrient limitation. *Front Microbiol* 2014; **5**: 1–10.

551 50. Snyder CH, Merbitz-Zahradnik T, Link TA, Trumpower BL. Role of the Rieske Iron – Sulfur Protein
552 Midpoint Potential in the Protonmotive Q-Cycle Mechanism of the Cytochrome bc 1 Complex. *J Bioenerg*
553 *Biomembr* 1999; **31**: 235–242.

554 51. Denke E, Merbitz-Zahradnik T, Hatzfeld OM, Snyder CH, Link TA, Trumpower BL. Alteration of the
555 midpoint potential and catalytic activity of the Rieske iron-sulfur protein by changes of amino acids forming

556 hydrogen bonds to the iron-sulfur cluster. *J Biol Chem* 1998; **273**: 9085–9093.

557 52. Hunte C, Solmaz S, Palsdóttir H, Wenz T. A structural perspective on mechanism and function of the
558 cytochrome bc1 complex. In: Schäfer G, Penefsky HS (eds). *Results and Problems in Cell Differentiation*.
559 2008. Springer Science+Business Media, pp 253–270.

560 53. Falkowski PG. Evolution of the nitrogen cycle and its influence on the biological sequestration of CO2 in
561 the ocean. *Nature* 1997; **387**: 272–275.

562 54. Kao WC, Hunte C. The molecular evolution of the Qo Motif. *Genome Biol Evol* 2014; **6**: 1894–1910.

563 55. Dibrova D V., Cherepanov DA, Galperin MY, Skulachev VP, Mulkidjanian AY. Evolution of cytochrome
564 bc complexes: From membrane-anchored dehydrogenases of ancient bacteria to triggers of apoptosis in
565 vertebrates. *Biochim Biophys Acta - Bioenerg* 2013; **1827**: 1407–1427.

566 56. White D. The physiology and biochemistry of prokaryotes, 3rd ed. 2000. Oxford University Press.

567 57. Thauer RK, Jungermann K, Decker K. Energy conservation in chemotrophic anaerobic bacteria. *Bacteriol*
568 *Rev* 1977; **41**: 100–180.

569 58. Giardina CP, Ryan MG. Total belowground carbon allocation in a fast-growing Eucalyptus plantation
570 estimated using a carbon balance approach. *Ecosystems* 2002; **5**: 487–499.

571 59. Edgar RC. MUSCLE: multiple sequence alignment with high accuracy and high throughput. *Nucleic Acids*
572 *Res* 2004; **32**: 1792–7.

573 60. Tamura K, Peterson D, Peterson N, Stecher G, Nei M, Kumar S. MEGA5: Molecular evolutionary genetics
574 analysis using maximum likelihood, evolutionary distance, and maximum parsimony methods. *Mol Biol*
575 *Evol* 2011; **28**: 2731–2739.

576 61. Stamatakis A. RAxML version 8: A tool for phylogenetic analysis and post-analysis of large phylogenies.
577 *Bioinformatics* 2014; **30**: 1312–1313.

578 62. Kelley LA, Mezulis S, Yates C, Wass M, Sternberg M. The Phyre2 web portal for protein modelling,
579 prediction, and analysis. *Nat Protoc* 2015; **10**: 845–858.

580 63. Dobin A, Davis CA, Schlesinger F, Drenkow J, Zaleski C, Jha S, et al. STAR: Ultrafast universal RNA-seq
581 aligner. *Bioinformatics* 2013; **29**: 15–21.

582 64. Liao Y, Smyth GK, Shi W. FeatureCounts: An efficient general purpose program for assigning sequence
583 reads to genomic features. *Bioinformatics* 2014; **30**: 923–930.

584 65. Love MI, Huber W, Anders S. Moderated estimation of fold change and dispersion for RNA-seq data with
585 DESeq2. *Genome Biol* 2014; **15**: 1–21.

586

587 **Figure legends**

588 **Figure 1**. (A) Maximum likelihood phylogenetic tree of NrfA amino acid sequences from known
589 respiratory ammonifiers and accompanying N-module composition for each organism. Pool
590 quinone is also noted for dual-pathway nitrite reducers and model species. Colors of the main
591 branches denote the 1st heme motif type: CxxCK and CxxCH. (B) Protein atomic composition
592 for N and C normalized to protein length for NirK and NrfA nitrite reductases. (C) State-
593 transition from ammonium-replete to ammonium-deplete for *I. calvum* C5 grown under 8mM
594 lactate 12mM nitrate minimal media at 30 ºC. Metabolite profiles for ammonium-deplete are
595 shown.

596

597 **Figure 2**. The effects of high resource (left; range of lactate concentrations with 12 mM NO_3^-)
598 and low resource (right; range of lactate concentrations with 1.2 mM NO_3^-) concentrations with
599 the same C:NO_3^- ratio on pathway selection in *I. calvum* C5. (A) Production of N_2O-N and net
600 change of NH_4^+ over a 100-hour incubation period at 30 ºC. Each bar represents the average of
601 8-10 replicates per treatment (Table S5). (B) Fraction of dissimilated N by pathway. (C) Growth
602 rates for each corresponding treatment. The x-axis label defines lactate concentration and C:NO_3^-
603 ratio in parentheses.

604

605 **Figure 3**. (A) Time-series metabolite profiles for lactate, nitrate, and nitrite (top pane),
606 production of dissimilated end-products as N_2O-N and net change in NH_4^+ ammonium
607 production (middle pane), and corresponding growth curve of *I. calvum* cells grown under 8 mM
608 lactate 12 mM nitrate (C:NO_3^- ratio = 2) (bottom pane). Sampling points during growth phases
609 are marked where transcriptomic profiling was performed (red arrows). (B) Metabolic
610 reconstruction of the ETC from *I. calvum* with transcriptional changes for genes participating in
611 dual-pathway dissimilatory nitrite reduction. Log_2 fold changes in transcript abundance are
612 shown for late exponential relative to early exponential growth phase (EE vs. LE), stationary
613 phase relative to early exponential growth phase (EE vs. ST), and stationary phase relative to late
614 exponential growth phase (LE vs. ST). Locus IDs for each gene product correspond to heat map
615 subplots in the order shown (left-to-right for each growth phase and top-to-bottom for each locus
616 ID specified). Higher transcript abundance is represented in red, lower transcript abundance in
617 blue, and no change in transcript abundance in white. Significant changes in transcript
618 abundance ($p < 0.01$) are marked as a red box. Value of log_2 fold change is specified within each
619 subplot. The log_2 fold changes of 14 NADH dehydrogenase subunits (Intca_03465-03530) were
620 averaged as transcriptional changes were all shifted in the same direction.

621

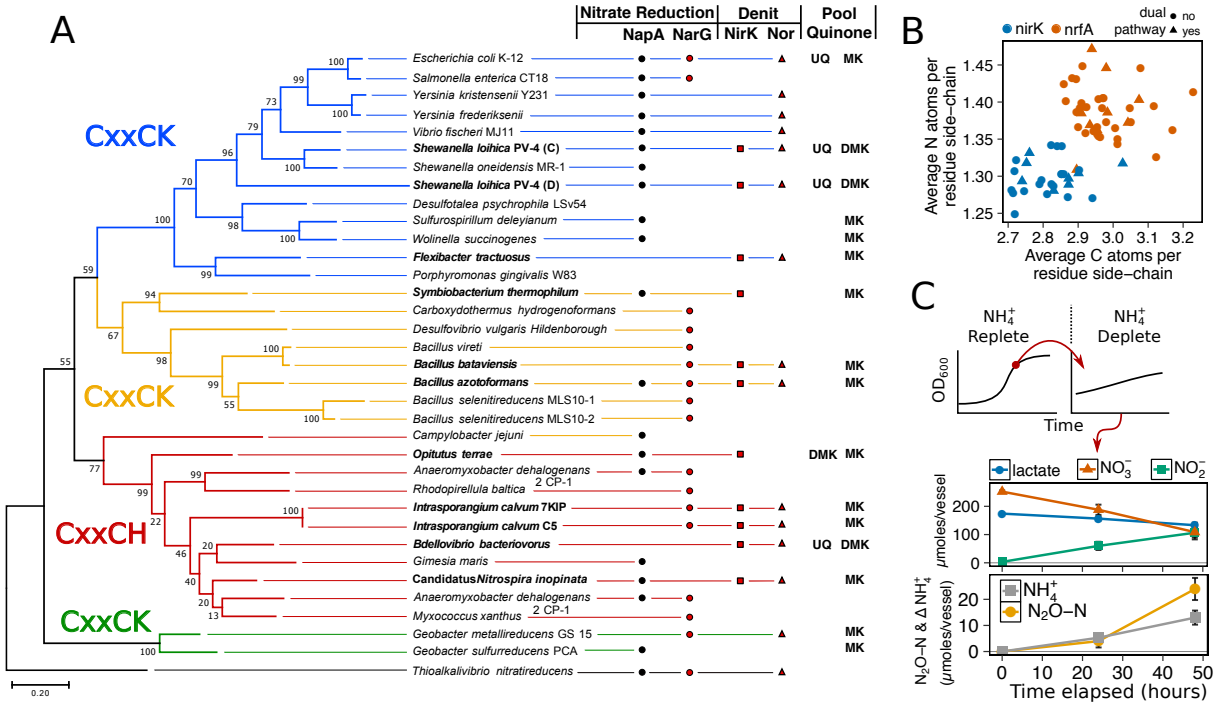

Figure 1. (A) Maximum likelihood phylogenetic tree of NrfA amino acid sequences from known respiratory ammonifiers and accompanying N-module composition for each organism. Pool quinone is also noted for dual-pathway nitrite reducers and model species. Colors of the main branches denote the 1st heme motif type: CxxCK and CxxCH. (B) Protein atomic composition for N and C normalized to protein length for NirK and NrfA nitrite reductases. (C) State-transition from ammonium-replete to ammonium-deplete for *I. calvum* C5 grown under 8mM lactate 12mM nitrate minimal media at 30 ºC. Metabolite profiles for ammonium-deplete are shown.

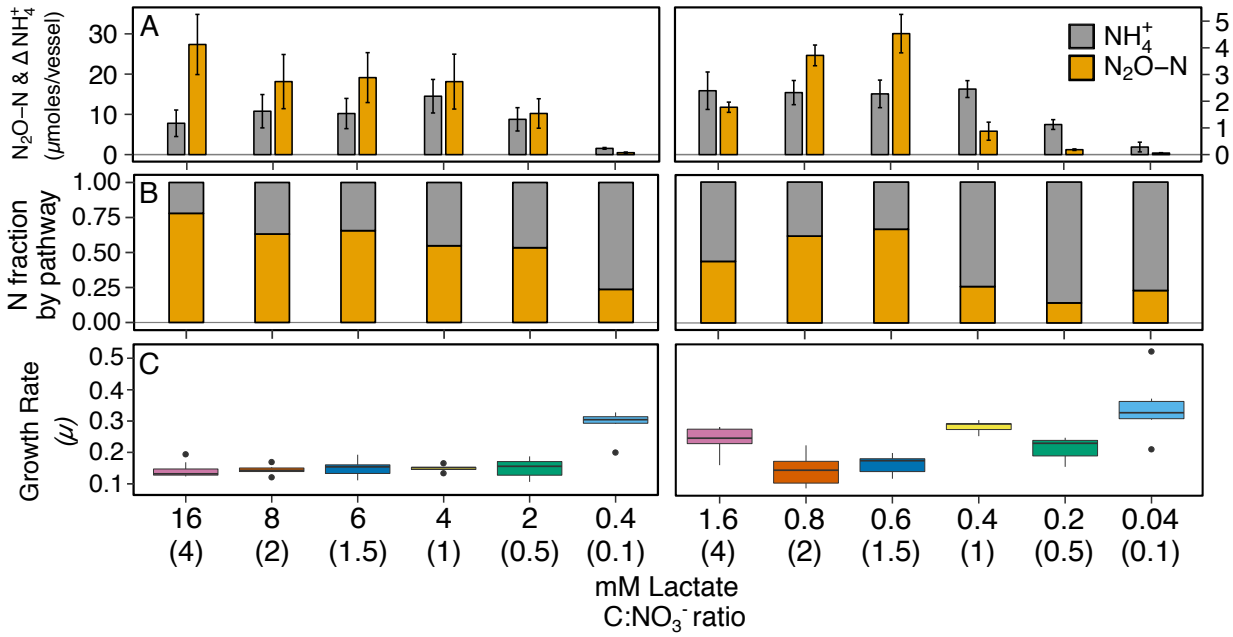

Figure 2. The effects of high resource (left; range of lactate concentrations with 12 mM NO_3^-) and low resource (right; range of lactate concentrations with 1.2 mM NO_3^-) concentrations with the same C:NO_3^- ratio on pathway selection in *I. calvum* C5. (A) Production of N_2O-N and net change of NH_4^+ over a 100-hour incubation period at 30 ºC. Each bar represents the average of 8-10 replicates per treatment (Table S5). (B) Fraction of dissimilated N by pathway. (C) Growth rates for each corresponding treatment. The x-axis label defines lactate concentration and C:NO_3^- ratio in parentheses.

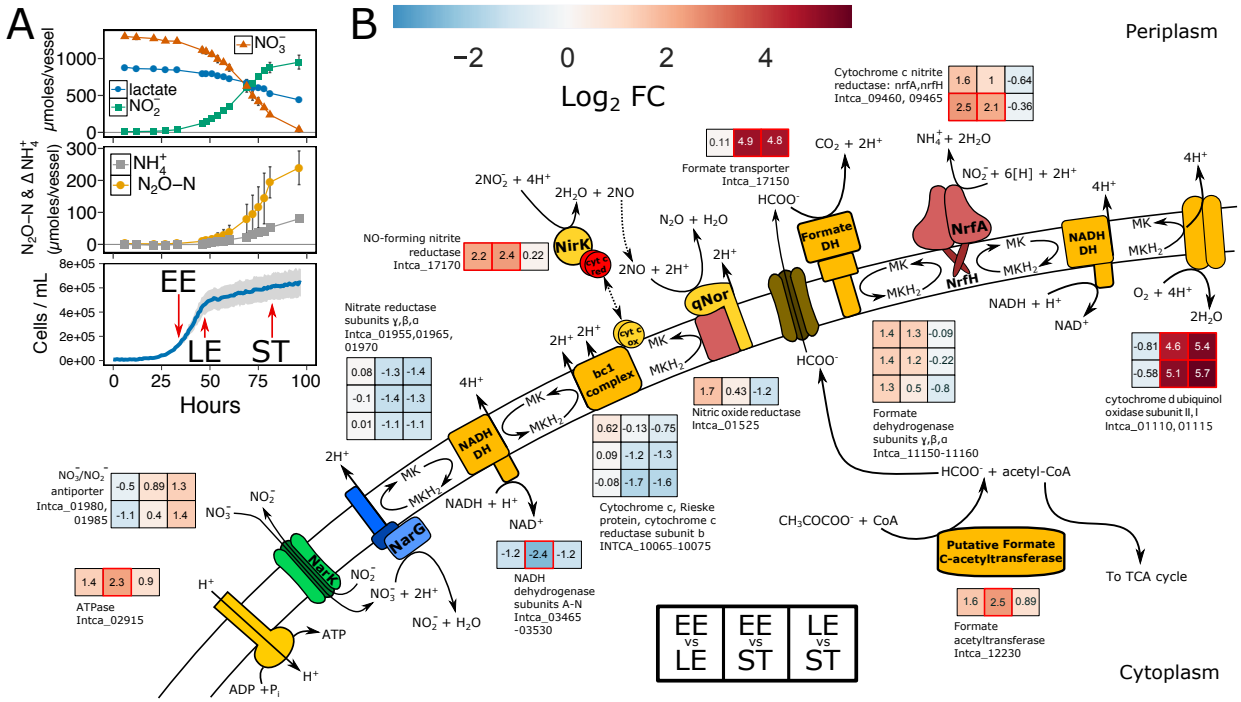

Figure 3. (A) Time-series metabolite profiles for lactate, nitrate, and nitrite (top pane), production of dissimilated end-products as N_2O-N and net change in NH_4^+ ammonium production (middle pane), and corresponding growth curve of *I. calvum* cells grown under 8mM lactate 12mM nitrate (C:NO_3^- ratio = 2) (bottom pane). Sampling points during growth phases are marked for transcriptomic analysis. (B) Metabolic reconstruction of the ETC from *I. calvum* with transcriptional changes for genes participating in dual-pathway dissimilatory nitrite reduction. Log_2 fold changes in transcript abundance are shown for late exponential relative to early exponential growth phase (EE vs. LE), stationary phase relative to early exponential growth phase (EE vs. ST), and stationary phase relative to late exponential growth phase (LE vs. ST). Locus IDs for each gene product correspond to heat map subplots in the order shown (left-to-right for each growth phase and top-to-bottom for each locus ID specified). Higher transcript abundance is represented in red, lower transcript abundance in blue, and no change in transcript abundance in white. Significant changes in transcript abundance ($p < 0.01$) are marked as a red box. Value of log_2 fold change is specified within each subplot. The log_2 fold changes of 14 NADH dehydrogenase subunits (Intca_03465-03530) were averaged as transcriptional changes were all shifted in the same direction.